RNA location and modeling of a WD40 repeat domain within the vault

**LAWRENCE B. KONG,[1] AMARA C. SIVA,[2] VALERIE A. KICKHOEFER,[2]
LEONARD H. ROME,[2] and PHOEBE L. STEWART[1]**

[1]Department of Molecular and Medical Pharmacology, Crump Institute for Biological Imaging, University of California at
 Los Angeles School of Medicine, A-324 CIBI, Los Angeles, California 90095-1770, USA
[2]Department of Biological Chemistry, UCLA School of Medicine, Los Angeles, California 90095-1737, USA

ABSTRACT

The vault complex is a ubiquitous 13-MDa ribonucleoprotein assembly, composed of three proteins (TEP1, 240 kDa; VPARP, 193 kDa; and MVP, 100 kDa) that are highly conserved in eukaryotes and an untranslated RNA (vRNA). The vault has been shown to affect multidrug resistance in cancer cells, and one particular component, MVP, is thought to play a role in the transport of drug from the nucleus. To locate the position of the vRNA, vaults were treated with RNases, and cryo-electron microscopy (cryo-EM) was performed on the resulting complexes. Using single-particle reconstruction techniques, 3,476 particle images were combined to generate a 22-Å-resolution structure. Difference mapping between the RNase-treated vault and the previously calculated intact vault reconstructions reveals the vRNA to be at the ends of the vault caps. In this position, the vRNA may interact with both the interior and exterior environments of the vault. The finding of a 16-fold density ring at the top of the cap has allowed modeling of the WD40 repeat domain of the vault TEP1 protein within the cryo-EM vault density. Both stoichiometric considerations and the finding of higher resolution for the computationally selected and refined "barrel only" images indicate a possible symmetry mismatch between the barrel and the caps. The molecular architecture of the complex is emerging, with 96 copies of MVP composing the eightfold symmetric barrel, and the vRNA together with one copy of TEP1 and four predicted copies of VPARP comprising each cap.

Keywords: β-propeller; cryo-electron microscopy; difference mapping; image reconstruction

INTRODUCTION

The vault complex is a ubiquitously expressed ribonucleoprotein particle found in eukaryotes as diverse as humans, mice, rabbits, Xenopus, sea urchins, and the slime mold *Dictyostelium discoideum* (Chugani et al., 1993). Initially, vaults were identified in preparations of clathrin-coated vesicles and named for their unique morphology (Kedersha & Rome, 1986a, 1986b). In mammals, vaults are located in the cytoplasm and exist in tens of thousands of copies per cell. Although the normal cellular function of the vault is not known, vault-expression levels have been found to correlate with the multidrug resistance properties observed in several cancer cell lines (Kickhoefer et al., 1998). It was shown by Kitazono et al. (1999) that within a cell, induction of the major vault protein (MVP), also known as the lung-

resistance related protein, has a direct influence on the nuclear uptake of the anticancer drug, doxorubicin. Increased MVP expression correlated with a decreased concentration of doxorubicin within the nucleus. Conversely, when the same cells were treated with a ribozyme against the MVP, the MVP levels were decreased, as the drug concentration within the nucleus increased. Nuclei isolated from cells with induced vault expression were found to efflux doxorubicin more rapidly, and efflux was blocked by antiMVP antibodies. This result is consistent with a role for the vault in some aspect of nucleocytoplasmic transport, as has been previously proposed (Chugani et al., 1993).

Vaults are the largest ribonucleoprotein particle known, with a mass of 12.9 ± 1 MDa as measured by STEM (Kedersha et al., 1991). The vault complex is composed of multiple copies of the MVP (p100), two high molecular-weight proteins (p240 and p193), and an untranslated vault RNA (vRNA) of 141 bases in rat (Kickhoefer et al., 1999a). Curiously, the vault p240 protein is identical to the mammalian telomerase-associated component, TEP1 (Kickhoefer et al., 1999b).

The N-terminal half of TEP1 contains four repeats of unknown function, an RNA-binding domain with three regions homologous to the *Tetrahymena* p80 protein, and an ATP/GTP-binding motif (Harrington et al., 1997; Nakayama et al., 1997). Using a yeast three-hybrid assay, TEP1 has been shown to interact with the telomerase RNA and various human-vault RNAs (Harrington et al., 1997; Kickhoefer et al., 1999b). The C-terminal third of TEP1 contains 16 WD40 repeats that have been proposed to play a role in the structural organization of the eightfold symmetric vault. Numerous members of the WD40 repeat family have been identified by sequence analysis (Neer et al., 1994) and the X-ray crystallographic structure of one is known, the β-subunit of the heterotrimeric G-protein complex (Wall et al., 1995). The vault p193 protein has been shown to have poly (ADP-ribose) polymerase (PARP) activity and thus has been named VPARP (Kickhoefer et al., 1999a). VPARP contains a BRCA1 COOH terminus (BRCT) domain, a region homologous to the catalytic domain of PARP, a region similar to the inter-α-trypsin inhibitor protein, and an MVP-interaction domain at the C-terminus. The MVP accounts for >70% of the vault mass and is thought to form the central barrel of the complex (Kedersha & Rome, 1986a; Kong et al., 1999). Freeze-etch images of opened vaults revealed eight rectangular petals per half vault, and stoichiometric calculations have assigned six copies of MVP to each petal, yielding 96 copies of MVP per vault (Kedersha et al., 1991). The vault RNA, which accounts for less than 5% of the total vault mass, has been cloned from several species and varies in length from 86 to 141 bases. The known mammalian vRNA sequences share ~80% identity as well as a common predicted secondary structure (Kickhoefer et al., 1993, 1998). Cryo-electron microscopy (cryo-EM) and single-particle reconstruction methods have produced a 31-Å-resolution structure of the intact vault (Kong et al., 1999).

Cryo-EM has proven useful for determining the molecular architecture of another ribonucleoprotein particle, the ribosome. Difference mapping of ribosome/tRNA has enabled localization of tRNA density to various binding sites (Agrawal et al., 1996; Stark et al., 1997a). The resolutions achieved by cryo-EM were sufficient to fit the X-ray crystallographic structures of the ribosomal L1 protein (Malhotra et al., 1998) and the elongation factor Tu (Stark et al., 1997b) within cryo-EM density. Other examples of cryo-EM difference mapping include localization of eight amino acid residues added to the N-terminus of the hepatitis B capsid protein (Conway et al., 1998) and isolation of the integrin receptor density within adenovirus/integrin complexes (Chiu et al., 1999). The ability of cryo-EM difference mapping to locate a component within a larger assembly is dependent upon the size of the component, its degree of structural order or variability, and the resolution of the analysis.

Here we present a reconstruction of the vault complex following RNase digestion of the vRNA at 22-Å resolution. A difference map between the structures of the published intact vault and the RNase-treated vault indicates the location of the vRNA within the complex. The improved resolution of the RNase-treated vault reconstruction enabled positioning of a model for the TEP1 WD40 domain within the cryo-EM density.

RESULTS

Purification of vaults and digestion of vault RNA

Vaults were isolated and purified from rat liver as previously described (Kong et al., 1999). To remove the RNA component from the vault complex, an unusually harsh treatment with two different RNA-degrading enzymes was required. Treatment with micrococcal nuclease alone was inefficient in removing the vRNA. Instead, high concentrations of both RNase T1 and RNase A were added to the isolated vaults. The RNase digestion reduced the levels of vRNA within the particle to below detectable levels, as measured by both SDS-PAGE gel electrophoresis and Northern blot analysis (Fig. 1). As the vRNA constitutes less than 5% of the total vault mass, the SDS-PAGE gel was overstained to clearly show the vRNA band before RNase treatment.

Cryo-EM imaging of RNase-treated vaults

RNase-treated vault particles were flash frozen on EM grids coated with holey carbon film as described in
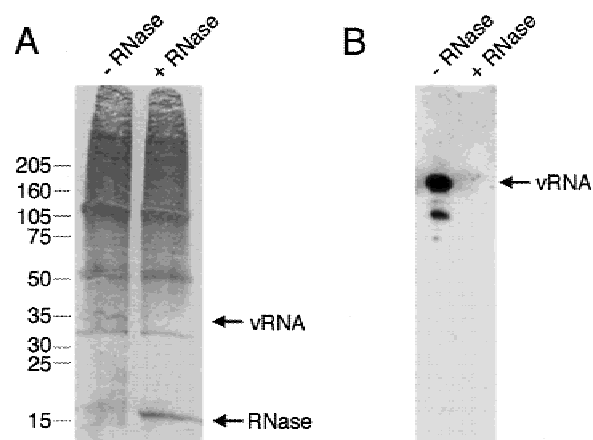

FIGURE 1. Treatment of the vault complex with RNase T1 and RNase A degraded the vault RNA below detectable levels. **A:** SDS-PAGE analysis of vault fractions before and after RNase treatment. The 37-kDa band in the −RNase lane corresponds to the vault RNA, and the ~15-kDa band in the +RNase lane is the result of the RNase that was added. The gel was overstained to clearly observe the vault RNA degradation. **B:** Northern blot analysis before and after RNase treatment using rat vault RNA as a probe. The presence of a weak second vRNA band in the Northern blot presumably corresponds to breakdown product.

Materials and methods. When imaged by low-dose cryo-EM, the RNase-treated vaults were well dispersed in the holes of the carbon support film (Fig. 2A). This made it relatively straightforward for one to collect a large number of particle images suitable for single-particle reconstruction. A data set of 4,317 RNase-treated vault particle images was extracted from 1,315 digital micrographs collected with a nominal magnification of 45,000×. In contrast, the intact vault particles that were previously studied tended to clump into large aggregates or stick to the carbon support film, making data collection more tedious. The published reconstruction of the intact vault particle was based on a smaller number of particle images, 1,352, and collected with a lower nominal magnification of 28,000×. The higher magnification of the RNase-treated vault images results in a smaller digital pixel size (4.1 Å on the sample scale) and reveals finer structural detail in the raw images. Three particularly clear end views are shown in Figure 2B, in which spikes can be seen around the

outer edge of the vault. Unfortunately, as the spikes blur together in some regions, it is difficult to count the exact number. Rotational power spectra of these images also do not give a clear result, but we estimate that there are roughly 48 spikes around the circumference of the vault.

Image processing for the RNase-treated vault

Eightfold symmetry for the vault has been inferred from freeze-etch images of particles that have opened into petal-like structures on polylysine-coated mica (Kedersha et al., 1991). During image processing for the intact vault particle, C8, or cyclic eightfold, symmetry was imposed, although dihedral eightfold (D8 or 822) symmetry could not be ruled out (Kong et al., 1999). The current data set of RNase-treated vault particle images was initially processed with C8 symmetry until a resolution of 26 Å was reached. At this point, the two ends of the vault appeared nearly identical, and from then on D8 symmetry was imposed.

To prevent the nonsymmetrically disposed contents trapped within the vault from interfering with the refinement process, we made use of a linearly ramped, elliptical mask (Fig. 3A). During each refinement cycle, we applied the elliptical mask to the reconstruction from the previous cycle and then projected it in a set of views spanning the asymmetric unit. These projection images served as an anchor set to refine the Euler orientational angles of the particle images. The elliptical mask was also applied to the two half reconstructions used for resolution assessment by Fourier shell correlation (FSC) methods. In this way, much of the disordered vault contents were excluded from the resolution assessment.

Based on the stoichiometry of the three vault proteins, we suspected that there might be a symmetry mismatch in the vault, with only the barrel portion following dihedral eightfold symmetry. After multiple refinement cycles and selection of the best subset of 3,476 particle images, the RNase-treated vault reconstruction reached a plateau of 23-Å resolution. To refine just the barrel midsection, we computationally selected the barrels from the subset of RNase-treated vault particle images. The selection was performed by nulling the barrel portion of the reconstruction, projecting the two caps in each of the 3,476 orientations, and then subtracting the cap projections from the RNase-treated vault particle images. The "barrel only" images underwent three rounds of refinement resulting in a 19-Å resolution reconstruction of the barrel. The spikes observed in some clear cryo-EM end views (Fig. 2B) were now apparent in slices through the widest portion of the barrel reconstruction. We estimate that the center-to-center distance for the spikes is ~24 Å, but the gaps between spikes are even smaller. When the barrel reconstruction is filtered to 19-Å resolution, the spikes
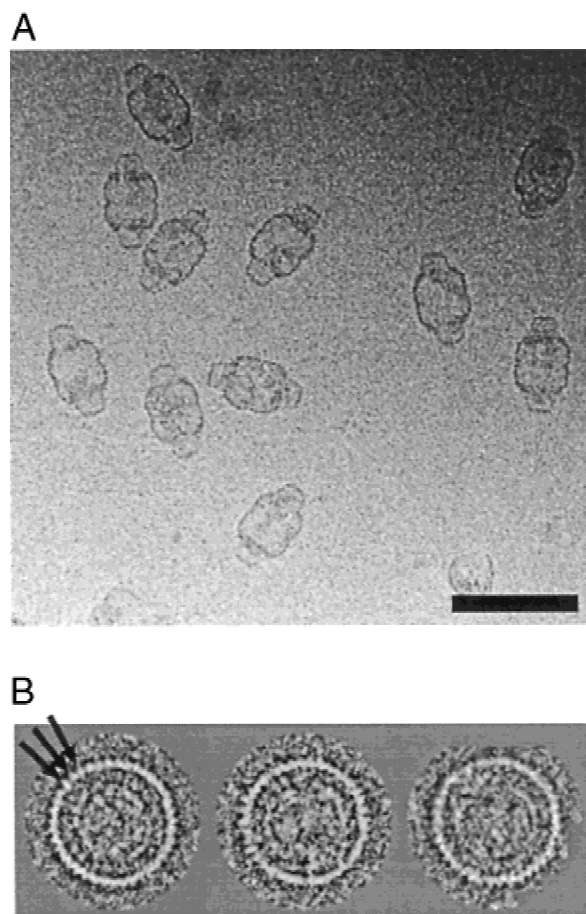

FIGURE 2. Cryo-EM images of the RNase-treated vault. **A:** A digital cryo-electron micrograph showing well-spaced RNase-treated vaults suspended in a layer of vitreous ice. The scale bar corresponds to 1,000 Å. **B:** Three end views of RNase-treated vault particles showing small spikes around the outer ring of density. Three clear spikes are marked by arrows. Note that the density has been inverted in these images, such that the particle is white.

are still discernible, but are partially merged together. Filtering to 23-Å resolution causes the spikes to completely merge. Thus, it seems reasonable that the spikes are not resolved in the 23-Å resolution RNase-treated vault reconstruction, but are resolved in the refined 19-Å resolution barrel reconstruction.

Reasoning that the caps might have hindered the refinement of the RNase-treated vault, we then applied the refined barrel only orientational angles to the particle images of the RNase-treated vault. The barrel portion of the final RNase-treated vault reconstruction appears virtually identical to the 19-Å resolution barrel only reconstruction. In Figure 3B we present a density slice through the spike region in the top half of the barrel and marked by an arrow in Figure 3A. This spike pattern continues for three density slices.

FSC plots for the final RNase-treated vault reconstruction, both with and without the elliptical mask applied, are shown in Figure 3C. Note that the mask shifts the FSC 0.5 threshold from 25- to 22-Å resolution. The elliptical mask was also used to reevaluate the resolution of the published intact vault reconstruction (Kong et al., 1999). With masking, the intact vault reconstruction has a resolution of 30 Å, which represents an improvement of 1 Å. As a test, the elliptical mask was applied to two noise maps and an FSC plot was generated. No appreciable correlation was observed, indicating that the elliptical mask does not produce an artificial enhancement in resolution, but rather serves to select for the density corresponding to the ordered vault shell. We presume that a symmetry mismatch within the caps lowers the overall resolution of the final RNase-treated vault reconstruction to 22 Å, and that the barrel portion of the reconstruction is really ~19-Å resolution.

The structure of the RNase-treated vault

The final RNase-treated vault reconstruction is presented in Figure 4 and overall, it appears quite similar to the published reconstruction of the intact vault. There are small holes in the density for the two caps, and the walls of the middle barrel-like section are quite smooth. A cropped view of the RNase-treated vault reveals the wall thickness to vary from 20 to 36 Å. As the minimum wall thickness is close to the resolution limit, it is possible that the actual vault walls are even thinner in some regions than they appear in the reconstruction. As observed previously, the volume of the barrel section corresponds almost exactly to that predicted for 96 copies of the major vault protein (Kong et al., 1999). Therefore, it is likely that 48 copies of the MVP form each half of the barrel and produce the spikes observed in the occasional end views and in the spike region of the reconstructed barrel.

The nearly smooth, featureless nature of the vault particle images could potentially lead to cylindrical av-

eraging of the density around the long axis of the vault. We suspected that the intact vault reconstruction was partially cylindrically averaged (Kong et al., 1999). Density slices of the higher-resolution RNase-treated vault reconstruction show features that indicate this structure is not cylindrically averaged. For comparison we calculated a test reconstruction from the same data set with randomized Φ angles and with imposed dihedral eightfold symmetry. The Φ angle corresponds to the rotation around the long axis of the particle. Corresponding density slices of the final RNase-treated vault reconstruction and the random Φ angle reconstruction are shown side by side in Figure 4B. All slices of the test reconstruction appear round, with even density around the periphery. In contrast, most slices through the final reconstruction show faceting and density variation around the circumference. This comparison, together with the observation of spikes within the reconstruction of the barrel, leads us to conclude that at least the barrel portion of the RNase-treated vault reconstruction is not cylindrically averaged.

Difference mapping to localize the vRNA

If the vRNA is ordered, then a difference map between the intact and RNase-treated vault reconstructions should reveal its location within the assembly. To compensate for the difference in resolution between the two reconstructions, the RNase-treated reconstruction was filtered to 30 Å before the subtraction. Only two significant regions of difference density were observed, with one region in each of the vault caps (Fig. 5). The clean subtraction of the rest of the vault density indicates that the loss of the vRNA does not cause a conformational change detectable at 30-Å resolution. The discrepancy in size between the difference density at the top and bottom of the vault may be attributed to the fact that D8 symmetry was imposed on the RNase-treated vault reconstruction, whereas only C8 symmetry was imposed on the intact vault. It is possible that different numbers of vRNA bind to each cap, but as single-particle reconstruction is based on image averaging, this question is difficult to resolve.

The volume of the observed difference density at just above the noise level corresponds to six copies of the rat vRNA per vault. Previous biochemical estimates indicate that vRNA accounts for 4.6% of the vault mass (Kedersha & Rome, 1986a), or that there are ~12 copies of vRNA per vault particle. If the bound vRNA does not follow the overall D8 symmetry of the vault particle, then the vRNA density would be smeared, or averaged, in the reconstruction. This would result in an underestimate of the vRNA copy number based on the volume of the difference density. Alternatively, it could well be that vaults have varying amounts of vRNA.
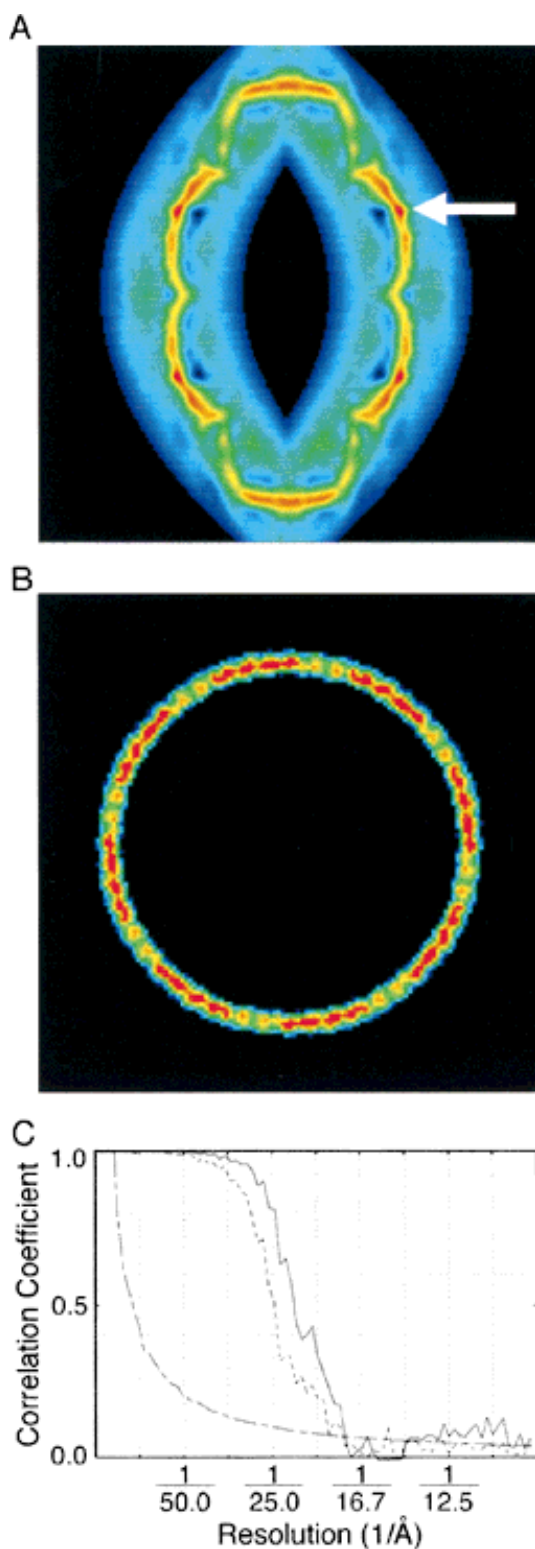
FIGURE 3. Elliptical masking and resolution assessment. **A:** The central slice of the RNase-treated vault reconstruction showing the applied elliptical mask. The white arrow marks the location of the spike region in the top half of the barrel. The strongest density is displayed in red and the weakest in blue. **B:** A slice through the spike region of the unfiltered final RNase-treated vault reconstruction showing a 48-fold repeat. Only density values above the isosurface level chosen for Figure 4 are displayed in color. **C:** FSC of the RNase-treated vault reconstruction both with (solid line) and without (short dashed line) the applied elliptical mask. A resolution of 22 Å is indi-
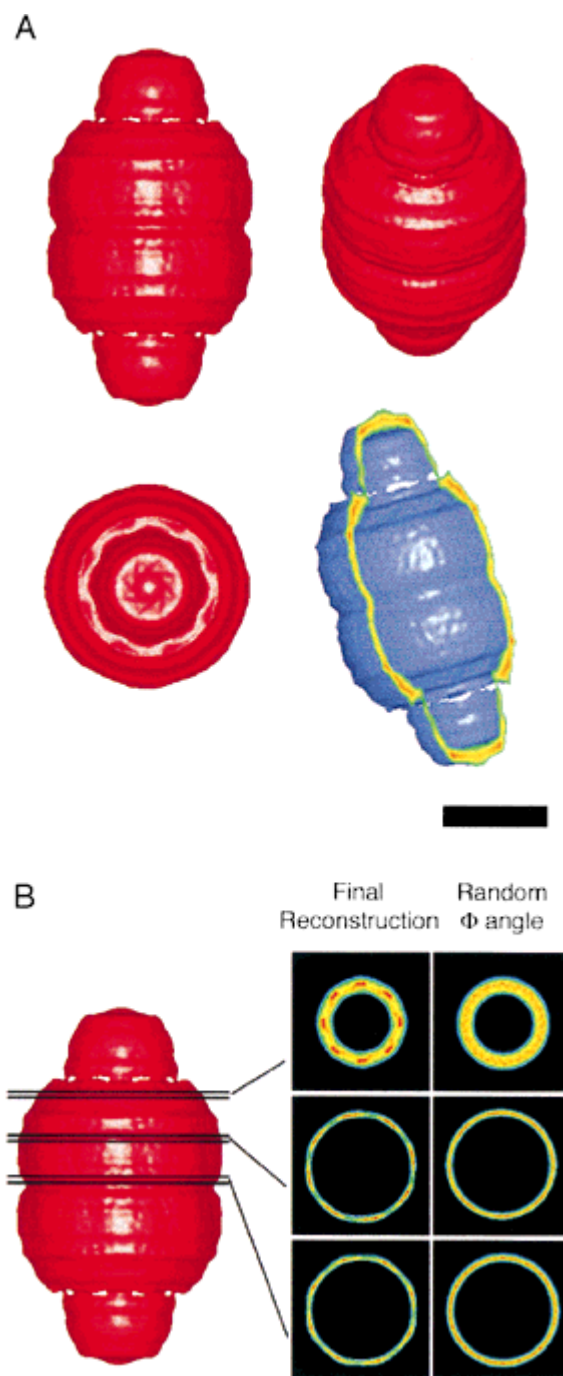
FIGURE 4. The final RNase-treated vault reconstruction. **A:** The full reconstruction (red) in three different views and a cropped view (blue). The density is isocontoured to account for 12.3 MDa of protein. The scale bar corresponds to 250 Å. **B:** Three slices through the barrel of the final reconstruction reveal features that vary around the circumference. The corresponding slices through the random Φ angle reconstruction are more rounded and show regular density with little variation. Both the final RNase-treated vault and the random Φ angle reconstructions are filtered to 22-Å resolution. The crop plane in **A** and the density slices in **B** are colored as in Figure 3.

cated at the 0.5 threshold level for the masked RNase-treated vault reconstruction. The long dashed line is a threshold curve, symmetry adjusted to 8.5 σ.

Internal contents of the vault

In addition to the main difference at the vault caps, there is also a subtle change in the weak internal density of the intact and RNase-treated vault reconstructions. As previously reported, density above the background noise level can be seen in the central slice of the intact vault reconstruction (Fig. 6A). The

FIGURE 6. Central slices from the intact (**A**) and RNase-treated (**B**) vault reconstructions. Note that less internal density is observed within the RNase-treated vault reconstruction. The color scales have been adjusted so that the vault barrels and backgrounds appear similar. The RNase-treated structure has weaker density at the ends of the vault caps because of the absence of the vRNA.

FIGURE 5. Difference imaging between the RNase-treated and intact vault reconstructions to reveal the location of the vRNA. The difference density above the noise level is shown in red, overlaid on two views of the intact vault reconstruction that has been cropped in half. Note that the difference density is located at the ends of the vault caps. The scale bar corresponds to 250 Å.
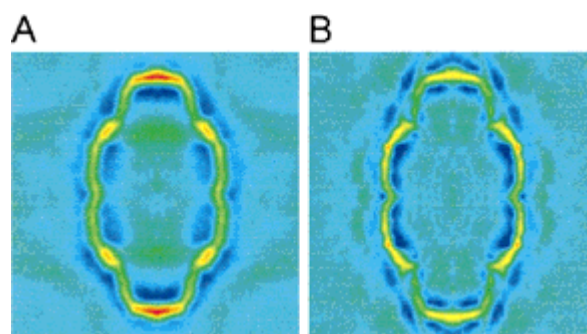
equivalent central slice of the RNase-treated vault reconstruction reveals less density in the vault cavity (Fig. 6B). Admittedly, different symmetries, C8 versus D8, were imposed on these two reconstructions. However, the C8 intact vault reconstruction has similar internal weak density in both halves of the vault, so the contents would probably not be too different with imposed D8 symmetry. The cryo-EM particle images of the RNase-treated vaults show that there is still significant density trapped within the vault (Fig. 2); therefore RNase treatment has not completely degraded the contents, but it might have partially degraded them. Comparison of the intact and RNase-treated vault reconstructions raises the possibility that some portion of the contents of the intact vault is RNA, either vRNA or another RNA species.

The molecular dimensions observed in the crystal structure of RNase T1 (Arni et al., 1988) suggest that this enzyme might fit through the small holes observed in the reconstruction ($\sim20 \times 40$ Å). Perhaps the smaller RNase A is able to pass through more easily. The size of the holes in the vault reconstruction is dependent on the isosurface value chosen, and at higher isosurface values, the holes appear larger. We have set the isosurface value of the RNase-treated reconstruction so that the volume corresponds with the average STEM mass measurement of the vault minus 5% for the vRNA. Also, we suspect that the caps do not follow perfect dihedral eightfold symmetry, and portions of the true cap structure may be blurred in the reconstruction. In support of this idea, we note that only the flat ends of the caps show strong density in the reconstruction, and the side walls of the caps appear weak as if they have been inappropriately averaged (Fig. 6B). So perhaps there are larger openings in the caps that are not observed in the symmetrized reconstruction, but that would allow both types of RNase molecules to enter the vault cavity.

Modeling of the vault protein TEP1 within the vault

Slices through the RNase-treated vault reconstruction were carefully analyzed for 16-fold density that might correspond to the 16-fold WD40 repeat within the TEP1 protein. A region of the cap, $\sim$12 Å thick, showed eight-fold density that can be further broken down into 16 radial spokes joined in pairs (Fig. 7A). In the crystallographic structure of the G-protein β-subunit, seven WD40 repeats form a sevenfold circular propeller structure, with each propeller blade formed by four β-strands (Wall et al., 1995). We took one of the propeller blades from the G-protein β-subunit structure and formed a 16-fold propeller, with the interblade spacing roughly preserved (Fig. 7B). The filtered 16-fold propeller model fits well within the 16-fold region of the cryo-EM density (Fig. 7C). The extra cryo-EM density that is not accounted for by the model may easily be explained by the other, unmodeled regions of TEP1, or alternatively, one of the other vault proteins. The 16-fold propeller model fits nicely within the top of the RNase-treated vault reconstruction, as can be seen in the cropped views of Figure 7D. Thus, we propose that there are two copies of the TEP1 protein within the vault, one in each cap.

DISCUSSION

Differences between the RNase-treated and intact vault reconstructions

To localize the vRNA within the vault particle, we have calculated a cryo-EM single-particle reconstruction of the RNase-treated vault as well as a difference map with the previously published intact vault reconstruction (Kong et al., 1999). We have found that a relatively harsh treatment with multiple RNases completely digests the vRNA while preserving the basic vault structure. The strongest density in the difference map is found at the ends of the two vault caps. Because the only molecular difference between the structures is the absence of vRNA in the RNase-treated vault, we conclude that the vRNA is located at these positions. The difference map suggests that the vRNA is intertwined with structural vault proteins, and this may explain why a harsh RNase treatment was necessary for digestion. The vRNA may be partially exposed on both the inner and outer surfaces of the vault. Exposure on the outside is consistent with our observation that intact vaults, but not RNase-treated vaults, appear to have an electrostatic attraction to the charged carbon support film of the EM grids. If the vRNA is exposed on the inner surface as the difference density suggests, then it might interact with the trapped internal contents of the vault. By comparing the central density slices of the two re-

constructions, it appears that either the RNase treatment has partially degraded the contents or that the contents are less well localized in the RNase-treated vault. Volume measurements suggest that there are at least six copies of vRNA per vault particle, but this could vary from particle to particle.

An unexpected benefit of the RNase treatment was that the vault particles were found more frequently in the holes of the carbon support film. This enabled us to collect more particle images and to use a higher magnification than used for imaging the intact vault. Both factors probably contributed to the higher resolution achieved for the RNase-treated vault, 22 Å. As we refined the RNase-treated vault structure, we found that the two ends of the vault were virtually identical, and thus we imposed D8 symmetry. As the trapped internal contents do not follow the same overall symmetry, we designed a three-dimensional elliptical mask that would isolate the strong protein shell of the vault. The elliptical mask was useful during refinement of the orientational angles as well for selecting the ordered regions for FSC resolution assessment.

Modeling of the TEP1 WD40 domain and its location near the vRNA

The RNase-treated vault reconstruction revealed a ring of density within the top of the vault cap with 16-fold symmetry. We postulated that this density might correspond to the 16-fold WD40 repeat of the TEP1 vault protein. In the absence of an atomic structure for TEP1, we modeled its WD40 region based on the β-propeller of the G-protein β-subunit (Wall et al., 1995). Many proteins have been found to contain a WD40 domain, and these most commonly have four to eight repeat sequences (Neer et al., 1994). It has been speculated that all proteins with WD repeats can form propeller structures, although not necessarily with the same number of blades (Garcia-Higuera et al., 1998). We currently have an atomic structure for only a sevenfold WD40 repeat protein, although the β-propeller structure has been observed often in other protein structures, and a high degree of structural similarity is found among them (Neer & Smith, 1996; ter Haar et al., 1998). Atomic structures are known for β-propellers containing from four up to eight repeats, with the additional blades of the higher repeats being accommodated by a larger overall diameter and subtle changes in the interblade spacing (Beisel et al., 1999). We designed a model for the TEP1 WD40 region with 16 blades within one ring, which fits well within the cryo-EM density.

The modeled position for the TEP1 WD40 ring is in the same region of the cap as the vRNA (Fig. 8). As the final RNase-treated vault reconstruction shows, there is no hole in the vault after degrading the vRNA. Also, the difference map positions the vRNA density within the ends of the caps rather than on the inner or outer
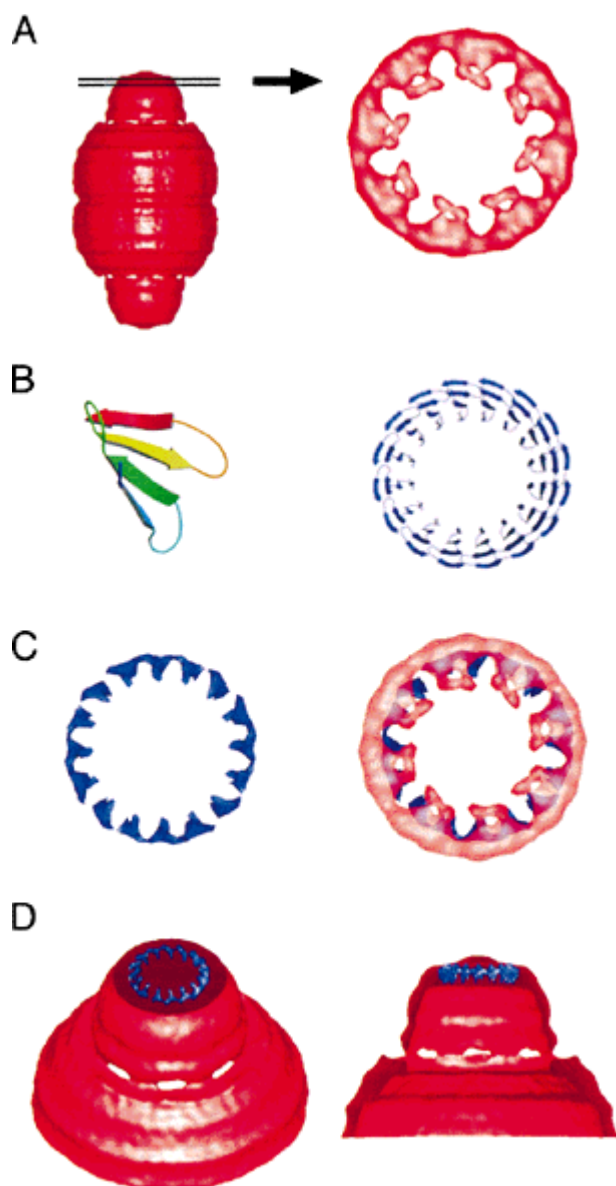
FIGURE 7. Modeling of the 16-fold TEP1 WD40 repeat. **A:** A density slab through the top of the vault cap reveals a ring of strong density in which 16 spokes are connected into pairs. **B:** Using a portion of the crystal structure of the heterotrimeric G-protein β-subunit (left), we modeled a 16-fold β-propeller (right), preserving the rough inter-blade spacing. **C:** The 16-fold atomic model was filtered to 18 Å (blue) and is shown overlaid onto the 16-spoke density of the vault cap (red). **D:** The 16-fold β-propeller is shown positioned within two cropped views of the reconstructed RNase-treated vault cap.

FIGURE 8. Colocalization of TEP1 and vRNA. A cropped view of the RNase-treated vault reconstruction (red) is shown with the model of the TEP1 WD40 domain (blue) and the vRNA density isolated from the difference map (yellow).

surface. Thus we speculate that the vRNA may be intertwined with the vault proteins in the cap, making the vRNA difficult to degrade, and, indeed, a harsh treatment with two ribonucleases was necessary. The co-localization of TEP1 and vRNA to the same region of the vault is consistent with the finding that TEP1 binds various RNA molecules, including three human vRNAs (Kickhoefer et al., 1999b).

Vault architecture and symmetry mismatch

Symmetry mismatches have been observed for other macromolecular assemblies, and the crystallographic structure of SV40 is a classic example (Liddington et al., 1991). In this virus, pentamers of the viral protein VP1 sit at sites of both local fivefold and sixfold symmetry, and conformationally variable C-terminal arms of VP1 adapt depending on the position of the pentamer within the capsid. Cryo-EM structural studies of the polymerase complex of bacteriophage phi6 (de Haas et al., 1999) and the ClpAP chaperone-assisted protease (Beuron et al., 1998) have also revealed symmetry mismatches. In the vault, the 16-fold WD40 domain of TEP1 accounts for ~25% of the protein sequence, and there are four N-terminal repeats that account for an additional ~5% (Nakayama et al., 1997). The remainder of the sequence does not indicate any other structural repeats. Thus the majority of TEP1 may have an asymmetric structure that is not properly represented in the reconstruction. Unless there are eight copies of VPARP per cap, the density of this protein may also be blurred or averaged in the reconstruction.

We propose a molecular architecture for the vault based on both structural and biochemical evidence. Unlike the barrel, the caps may not follow perfect dihedral eightfold symmetry throughout. A single copy of TEP1 per cap is presumed from our observation that one 16-fold β-propeller snugly fits within the end of the vault cap. The VPARP copy number is deduced from the STEM mass measurement for the intact vault, 12.9 ± 1 MDa, after subtracting the mass attributed to MVP, TEP1, and vRNA (9.6 MDa for 96 copies of MVP, 480 kDa for two copies of TEP1, and 645 kDa or 5% of the total mass for the vRNA). The remaining 2.2 ± 1 MDa

indicates 11 ± 5 copies of VPARP (193 kDa each) in the vault. The relatively large error range in the STEM mass measurement makes it difficult to arrive at a precise copy number for VPARP. Interpretation of the STEM measurement is further complicated by the fact that it includes the average mass of the contents within the vault, which we estimate from the cryo-EM particle images, is roughly 1 MDa.

Analysis of the TEP1 sequence suggested to us that perhaps the four N-terminal repeats of unknown function serve to bind four copies of VPARP. Also, it is easier to envision four, rather than three, five, six, or seven copies of VPARP interacting with the eightfold barrel. The upper limit estimated from the STEM mass measurement is eight copies of VPARP per cap, but this does not allow for the mass of the vault contents or account for the suggestion of a symmetry mismatch between the caps and the barrel. Therefore we propose a model for the vault with the barrel composed of 96 copies of MVP, and each cap containing one copy of TEP1, four copies of VPARP, and three or more copies of vRNA. An improved understanding of the vault structure will be required to resolve how the symmetry mismatches are accommodated and how this unusual complex assembles.

MATERIALS AND METHODS

Sample preparation

Vaults were purified as previously described (Kong et al., 1999). Final purified vaults from the CsCl load fraction were resuspended in MES buffer [0.09 MES, 0.01 M sodium phosphate, 1.0 M $MgCl_2$, 0.5 mM EGTA, 0.02% sodium azide (pH 6.5) and protease inhibitor cocktail]. Approximately 160 μg of CsCl purified vaults were incubated with 100 U/mL of RNase T1 (Ambion) and 100 μg/mL of RNase A for 2 h at 37 °C. The combination of a large amount of two RNases was necessary to degrade the vRNA to below detectable levels. Use of micrococcal nuclease was ineffective in the degradation of the vRNA as verified with Northern blot analysis (data not shown). Vaults are stable for a minimum of four weeks when stored at 4 °C.

Assay for removal of vRNA

For SDS-PAGE analysis, ~40 μg of untreated and RNase-treated vaults were run on a 4–15% gradient gel and silver stained. The band at 37 kDa in the intact vault lane represents the vRNA (Fig. 1A). For Northern blot analysis, samples from RNase-treated and untreated CsCl purified vaults (~80 μg each) were isolated through phenol/chloroform extraction, and ethanol precipitation with 5 μg *Escherichia coli* tRNA added as a carrier. The resulting pellets were resuspended in RNA loading dye and run on a 10% acrylamide/8 M urea TBE (Tris-Borate-EDTA) gel and electroblotted to a Zeta-Probe GT membrane (Biorad). The membrane was hybridized with a randomly primed rat vRNA probe as described previously (Kickhoefer et al., 1993). As the vaults are

normally stored in MES buffer, which is usable for RNase digestions, there was not an appreciable dilution in sample volume, and reconcentration of the RNase-treated vault sample was not required prior to cryo-plunging. Reactive bands were visualized by exposure to a Molecular Dynamics PhosphorImager screen.

Cryo-electron microscopy

Electron microscope grid preparation and cryo-plunging were performed as previously described (Adrian et al., 1984). A 4-μL droplet of concentrated vaults was applied to a glow-discharged holey carbon grid, blotted briefly, and plunged into ethane slush chilled by liquid nitrogen. The grids were transferred under liquid nitrogen to a Gatan 626 cryo-transfer holder and examined in a Philips CM120 Transmission Electron Microscope equipped with a LaB_6 filament, Gatan cryo-accessories, and a Gatan slow-scan CCD camera (1024×1024 pixels, YAG scintillator). Images were collected under low dose conditions (<20 electrons/$Å^2$), at a nominal magnification of 45,000×, and with two different underfocus values (1.0 μm and 0.6 μm). The digital micrographs had a pixel size of 4.1 Å on the sample scale, as determined by calibration with a catalase crystal.

Image processing

All processing was performed on either Digital Equipment Corporation/Compaq alpha workstations or a Silicon Graphics Reality Monster supercomputer with 32 processors, all with UNIX operating systems. Individual vault particle images were extracted from raw digital micrographs into 200×200 pixel fields using the QVIEW software package (Shah & Stewart, 1998). This package enabled background subtraction and particle selection with an elliptical mask. The IMAGIC software package was used for all subsequent reconstruction procedures (van Heel et al., 1996). A preliminary set of 1,213 particle images from 312 micrographs collected at 1 μm underfocus were used to calculate Euler angles, using the angular reconstitution method and assuming C8 symmetry. An initial reconstruction was generated using the exact filtered back projection algorithm (Hamming filter factor of 0.75).

An anchor set of 140 projections was produced from the initial reconstruction with a 7.5° spacing and evenly spanning the C8 asymmetric unit of the Euler sphere. These projections were used to find the Euler angles of the 1,335 particle images collected at 1 μm underfocus and 1,444 particle images collected at 0.6 μm underfocus. The 1 μm and 0.6 μm underfocus particle images were combined following correction of the two-dimensional particle images for the contrast transfer function (CTF). The parameters used for the CTF were $C_s = 2$ mm, fraction of amplitude contrast = 0.1, kV = 120, decay constant = 10 nm^2, Fermi filter resolution cutoff = 8.15 Å, filter width = 5 Å, and underfocus = 1.0 μm or 0.6 μm. The resulting CTF equations were compared with the radial power spectra of the sum of the particle images at either defocus value. Although the power spectra were not clear enough to fit all of the CTF parameters, they did confirm the zero positions.

Three rounds of anchor set refinement were performed with a 7.5° anchor spacing, a 2° angle refinement step size,

and with imposed C8 symmetry. Three additional rounds of refinement followed imposing D8 symmetry. For the last round, the angular refinement, the angle refinement step size was 1°. The resolution, as assessed by the FSC 0.5 threshold, reached a plateau 23 Å. Before calculating the next reconstruction, we used two criteria (the error per particle produced during filtered back projection and the cross-correlation coefficient generated between the original images and reprojections of the reconstruction) to select for the particle images with the highest correlation to the rest of the data set and remove the worst 20% of the particle images. This selection process did not improve the resolution at the FSC 0.5 threshold; however, it did reveal some agreement in the data set at 20-Å resolution with a correlation of 0.2.

To refine the barrel only portion of the vaults, we computationally selected the barrels from RNase-treated vault particle images. This was accomplished by first nulling the barrel portion of the RNase-treated vault reconstruction in IMAGIC. Projections of the two remaining caps were then generated using the orientational angles for the RNase-treated vault particle images. Subtraction of the cap projections from the vault particle images produced barrel only images. Additionally, the two caps were nulled in the RNase-treated vault reconstruction to create a barrel only model. The orientational angles for the barrel only images were refined with D8 symmetry using a 7.5° anchor set spacing and a 2° angle refinement step size in rounds 1 and 2. For the third round of refinement, the anchor set spacing was reduced to 4° and the angle refinement step size to 1°. The refined orientational angles for the barrel only images were used to calculate the final reconstruction of the RNase-treated vault.

A linear ramped elliptical mask was utilized to remove the disordered vault contents and external noise around the particle during most of the refinement and for the FSC resolution assessment tests. The inner ellipse had short and long radii of 151 and 306 Å, respectively, whereas the outer ellipse had short and long radii of 224 and 413 Å, respectively, where the long axes coincide with the long axis of the vault. The final reconstruction was displayed using the AVS (Advanced Visualization Systems, Inc.) software package. The reconstruction was contoured at an isosurface corresponding to a molecular mass of 12.9 MDa for the intact vault, and 12.3 MDa for the RNase-treated vault, assuming a protein density of 1.39 g/cm^3. The difference in density between protein and RNA (1.71 g/cm^3) was not taken into consideration, given the small (~5%) percentage of mass due to the vRNA. As the absolute hand of the vault particle has not been determined, an arbitrary hand is displayed.

The random Φ angle reconstruction was created using a UNIX script to replace each calculated Φ angle with a random number generated between 0.0 and 45.0. The Φ angle denotes the rotation about the eightfold axis. A reconstruction with imposed D8 symmetry was calculated preserving the correct Θ and Ω orientational angles.

Difference mapping between the intact and RNase-treated vault structures

The three-dimensional reconstructions of the intact and RNase-treated vaults were both filtered to 30 Å, and the density was normalized. Subtraction of the RNase-treated vault from the intact vault was performed using IMAGIC. A

reconstruction of the RNase-treated vault using a subset of the data corresponding to the same number of particles as used in the intact vault reconstruction yielded similar findings for the vRNA density and the internal contents. In estimating the copy number for vRNA from the difference density, we used an RNA density value of 1.71 g/cm^3.

Modeling of the WD40 repeat of TEP1

A single blade from the β-propeller of the heterotrimeric G-protein β-subunit (residues 188–222 from β-subunit; Protein Data Bank Identification code 1GP2) was used to build a 16-bladed model. The spacing of the blades was kept roughly equivalent to the blade spacing in the G-protein β-subunit. The atomic model was filtered to 18-Å resolution and mapped onto the vault structure using AVS.

ACKNOWLEDGMENTS

REFERENCES

Adrian M, Dubochet J, Lepault J, McDowall AW. 1984. Cryo-electron microscopy of viruses. *Nature 308*:32–36.

Agrawal RK, Penczek P, Grassucci RA, Li Y, Leith A, Nierhaus KH, Frank J. 1996. Direct visualization of A-, P-, and E-site transfer RNAs in the *Escherichia coli* ribosome. *Science 271*:1000–1002.

Arni R, Heinemann U, Tokuoka R, Saenger W. 1988. Three-dimensional structure of the ribonuclease T1 2′-GMP complex at 1.9-Å resolution. *J Biol Chem 263*:15358–15368.

Beisel HG, Kawabata S, Iwanaga S, Huber R, Bode W. 1999. Tachylectin-2: Crystal structure of a specific GlcNAc/GalNAc-binding lectin involved in the innate immunity host defense of the Japanese horseshoe crab *Tachypleus tridentatus*. *EMBO J 18*:2313–2322.

Beuron F, Maurizi MR, Belnap DM, Kocsis E, Booy FP, Kessel M, Steven AC. 1998. At sixes and sevens: Characterization of the symmetry mismatch of the ClpAP chaperone-assisted protease. *J Struct Biol 123*:248–259.

Chiu CY, Mathias P, Nemerow GR, Stewart PL. 1999. Structure of adenovirus complexed with its internalization receptor, $\alpha v \beta 5$ integrin. *J Virol 73*:6759–6768.

Chugani DC, Rome LH, Kedersha NL. 1993. Evidence that vault ribonucleoprotein particles localize to the nuclear pore complex. *J Cell Sci 106*:23–29.

Conway JF, Cheng N, Zlotnick A, Stahl SJ, Wingfield PT, Steven AC. 1998. Localization of the N terminus of hepatitis B virus capsid protein by peptide-based difference mapping from cryoelectron microscopy. *Proc Natl Acad Sci USA 95*:14622–14627.

de Haas F, Paatero AO, Mindich L, Bamford DH, Fuller SD. 1999. A symmetry mismatch at the site of RNA packaging in the polymer-

ase complex of dsRNA bacteriophage phi6. *J Mol Biol 294*:357–372.

Garcia-Higuera I, Gaitatzes C, Smith TF, Neer EJ. 1998. Folding a WD repeat propeller. Role of highly conserved aspartic acid residues in the G protein beta subunit and Sec13. *J Biol Chem 273*:9041–9049.

Harrington L, McPhail T, Mar V, Zhou W, Oulton R, Bass MB, Arruda I, Robinson MO. 1997. A mammalian telomerase-associated protein. *Science 275*:973–977.

Kedersha NL, Heuser JE, Chugani DC, Rome LH. 1991. Vaults. III. Vault ribonucleoprotein particles open into flower-like structures with octagonal symmetry. *J Cell Biol 112*:225–235.

Kedersha NL, Rome LH. 1986a. Isolation and characterization of a novel ribonucleoprotein particle: Large structures contain a single species of small RNA. *J Cell Biol 103*:699–709.

Kedersha NL, Rome LH. 1986b. Preparative agarose gel electrophoresis for the purification of small organelles and particles. *Anal Biochem 156*:161–170.

Kickhoefer VA, Rajavel KS, Scheffer GL, Dalton WS, Scheper RJ, Rome LH. 1998. Vaults are up-regulated in multidrug-resistant cancer cell lines. *J Biol Chem 273*:8971–8974.

Kickhoefer VA, Searles RP, Kedersha NL, Garber ME, Johnson DL, Rome LH. 1993. Vault ribonucleoprotein particles from rat and bullfrog contain a related small RNA that is transcribed by RNA polymerase III. *J Biol Chem 268*:7868–7873.

Kickhoefer VA, Siva AC, Kedersha NL, Inman EM, Ruland C, Streuli M, Rome LH. 1999a. The 193-kD vault protein, VPARP, is a novel poly(ADP-ribose) polymerase. *J Cell Biol 146*:917–928.

Kickhoefer VA, Stephen AG, Harrington L, Robinson MO, Rome LH. 1999b. Vaults and telomerase share a common subunit, TEP1. *J Biol Chem 274*:32712–32717.

Kitazono M, Tomoyuki S, Takebayashi Y, Chen Z, Furakawa T, Nagayama S, Tani A, Takao S, Aikou T, Akiyama S. 1999. Multidrug resistance and the lung resistance-related protein in human colon carcinoma SW-620 cells. *J Natl Cancer Inst 91*:1647–1653.

Kong LB, Siva AC, Rome LH, Stewart PL. 1999. Structure of the vault, a ubiquitous cellular component. *Structure 7*:371–379.

Liddington RC, Yan Y, Moulai J, Sahli R, Benjamin TL, Harrison SC. 1991. Structure of simian virus 40 at 3.8-Å resolution. *Nature 354*:278–284.

Malhotra A, Penczek P, Agrawal RK, Gabashvili IS, Grassucci RA, Jünemann R, Burkhardt N, Nierhaus KH, Frank J. 1998. *Escherichia coli* 70 S ribosome at 15 Å resolution by cryo-electron microscopy: Localization of fMet-tRNAfMet and fitting of L1 protein. *J Mol Biol 280*:103–116.

Nakayama J, Saito M, Nakamura H, Matsuura A, Ishikawa F. 1997. TLP1: A gene encoding a protein component of mammalian telomerase is a novel member of WD repeats family. *Cell 88*:875–884.

Neer EJ, Schmidt CJ, Nambudripad R, Smith TF. 1994. The ancient regulatory-protein family of WD-repeat proteins. *Nature 371*:297–300.

Neer EJ, Smith TF. 1996. G protein heterodimers: New structures propel new questions. *Cell 84*:175–178.

Shah AK, Stewart PL. 1998. QVIEW: Software for rapid selection of particles from digital electron micrographs. *J Struct Biol 123*:17–21.

Stark H, Orlova EV, Rinke-Appel J, Jünke N, Mueller F, Rodnina M, Wintermeyer W, Brimacombe R, van Heel M. 1997a. Arrangement of tRNAs in pre- and posttranslocational ribosomes revealed by electron cryomicroscopy. *Cell 88*:19–28.

Stark H, Rodnina MV, Rinke-Appel J, Brimacombe R, Wintermeyer W, van Heel M. 1997b. Visualization of elongation factor Tu on the *Escherichia coli* ribosome. *Nature 389*:403–406.

ter Haar E, Musacchio A, Harrison SC, Kirchhausen T. 1998. Atomic structure of clathrin: A beta propeller terminal domain joins an alpha zigzag linker. *Cell 95*:563–573.

van Heel M, Harauz G, Orlova EV. 1996. A new generation of the IMAGIC image processing system. *J Struct Biol 116*:17–24.

Wall MA, Coleman DE, Lee E, Iñiguez-Lluhi JA, Posner BA, Gilman AG, Sprang SR. 1995. The structure of the G protein heterotrimer G_I alpha 1 beta 1 gamma 2. *Cell 83*:1047–1058.